Applied Catalysis B: Environmental 236 (2018) 107–116

Contents lists available at ScienceDirect

Applied Catalysis B: Environmental

journal homepage: www.elsevier.com/locate/apcatb

An Effective Way to Improve Bifunctional Electrocatalyst Activity of Manganese Oxide via Control of Bond Competition

Bohyun Kang[a,1], Xiaoyan Jin[a,1], Seung Mi Oh[a], Sharad B. Patil[a], Min Gyu Kim[b], Sun Hee Kim[c], Seong-Ju Hwang[a,*]

[a] Center for Hybrid Interfacial Chemical Structure (CICS), Department of Chemistry and Nanoscience, College of Natural Sciences, Ewha Womans University, Seoul 03760, Republic of Korea
[b] Pohang Light Source, Pohang 37673, Republic of Korea
[c] Western Seoul Center, Korea Basic Science Institute, Seoul 03759, Republic of Korea

ARTICLE INFO

Keywords:
Bifunctional electrocatalysts
Manganese oxide
Bond competition
Oxygen evolution reaction
Oxygen reduction reaction

ABSTRACT

A critical role of bond competition in tailoring Mn valence state and bifunctional electrocatalyst activity of manganese oxide is evidenced by the remarkable improvement of the electrocatalyst activity of α-MnO_2 upon the partial substitution of electronegative Ru^{4+} ion. The replacement of Mn^{4+} ion with more electronegative Ru^{4+} one is quite effective in weakening adjacent (Mn − O) bonds in terms of bond competition, leading to the stabilization of Jahn-Teller active Mn^{3+} species, as well as in providing electrocatalytically active Ru sites. The resulting Ru-substituted α-$Mn_{1-x}Ru_xO_2$ nanowires show much higher electrocatalyst activities for both oxygen evolution reaction (OER) and oxygen reduction reaction (ORR) than does the physical mixture of α-MnO_2 and RuO_2, indicating the main role of (Mn − O) bond covalency in the optimization of the bifunctional electrocatalyst activity of manganese oxide. The present study underscores that, like the previous strategy of structural disorder enhancement, the substitution of highly electronegative cation can provide a novel efficient way of improving the electrocatalyst performance of manganese oxide via the bond competition between adjacent (Ru − O) and (Mn − O) bonds.

1. Introduction

Electrocatalysts for oxygen evolution reaction (OER) and oxygen reduction reaction (ORR) attract intense research interest because of their critical roles in many emerging energy technologies such as fuel cells, metal − air batteries, water electrolyzers, photoelectrochemical cells, and so on [1–4]. Since both the oxidative and reductive transformations between O^{2-} and O_2 require the simultaneous transfer of four electrons, it is not easy to explore efficient electrocatalysts for these sluggish reactions [5,6]. Even though noble metals like Pt and Ir show promising performance as electrocatalysts, their high price and limited abundance frustrate the commercialization of these materials [7]. Also, these noble metal-based electrocatalysts are active only for either OER or ORR, although the application as electrode for metal − air batteries demands bifunctional electrocatalyst active for both the reactions [8]. As an alternative electrocatalyst, transition metal oxides receive special attention because of their remarkable cost-effective advantages over noble metal [9,10]. Among diverse metal oxides, α-MnO_2-structured manganese oxide boasts remarkable cost-effectiveness and environmental friendliness as well as promising bifunctional electrocatalytic activity for both OER and ORR [10]. Yet, the electrocatalytic activity of α-MnO_2 is still far poorer than those of commercial Pt/C and Ir/C [11]. Both the OER and ORR processes induced by manganese oxide involve reversible cycling among Mn^{2+}, Mn^{3+}, and Mn^{4+} oxidation states as well as surface adsorption/desorption process of oxygen species [12]. Since Jahn-Teller active Mn^{3+} ion is the most unstable Mn oxidation state [12], it is of crucial importance to stabilize this species for improving the electrocatalyst performance of MnO_2 [13,14]. There are several attempts to stabilize this unstable Mn^{3+} species by increasing the structural deformation of MnO_2 lattice [15]. In one instance, the Cu^{2+} doping for α-MnO_2 induces the formation of surface Mn^{3+} ion due to the increase of surface defect [16]. Although an enhanced distortion of local symmetry around Mn ion is effective in improving the stability of Mn^{3+} ion [17], the increased structural distortion would have detrimental effect on the electrical conductivity of manganese oxide and thus its electrocatalyst activity. Alternatively, the tuning of bond competition between neighboring (metal − O) bonds can provide another way of stabilizing a specific oxidation state of metal

* Corresponding author.
E-mail address: hwangsju@ewha.ac.kr (S.-J. Hwang).
[1] These authors contributed equally to this work.

https://doi.org/10.1016/j.apcatb.2018.05.010
Received 7 August 2017; Received in revised form 6 April 2018; Accepted 4 May 2018
Available online 05 May 2018
0926-3373/

ion; the highly covalent (metal − O) bond leads to the weakening of adjacent (metal' − O) bond and the stabilization of low-valent metal' ion due to the decrease of the bond covalency [18]. Thus, the partial substitution of electronegative metal ion into the α-MnO_2 lattice can stabilize unstable Jahn-Teller active Mn^{3+} ion via the creation of the tetragonal distortion of MnO_6 octahedra with elongated (Mn − O) bond distance. Simultaneously, the elongation of (Mn − O) bond distance can facilitate the surface adsorption of oxygen species on manganese oxide. Judging from the high electronegativity of Ru^{4+} ion and the excellent electrical conductivity and high OER electrocatalytic activity of RuO_2 material [19], Ru^{4+} ion can be one of the most promising substituents for stabilizing unstable Mn^{3+} state in α-MnO_2 lattice and thus enhancing the electrocatalytic activity of α-MnO_2 material. Yet, at the time of this submission, we are unaware of any other report about the optimization of Mn valency and electrocatalyst performance of manganese oxides in terms of the tuning of bond competition.

In the present study, the (Mn − O) bond covalency, Mn valence state, and electrocatalyst activity of α-MnO_2 nanowire can be tailored by the partial substitution of Ru^{4+} ion through the bond competition. The effects of Ru substitution on the crystal structures, morphologies, and chemical bonding nature of α-$Mn_{1-x}Ru_xO_2$ 1D nanowires are systematically investigated. The obtained α-$Mn_{1-x}Ru_xO_2$ nanowires are applied as bifunctional electrocatalysts for both OER and ORR to probe the influence of Ru substituent on the electrocatalytic activity of manganese oxide.

2. Experimental

2.1. Sample preparation

The Ru-substituted α-$Mn_{1-x}Ru_xO_2$ nanowires were synthesized by the one-pot hydrothermal reaction for the ion-adduct of $MnO_4^- - Ru^{3+}$ as follows [20]; 0.5 g of $KMnO_4$, 0.2 g of $MnSO_4{\cdot}H_2O$, and 0.048 − 0.23 g of $RuCl_3{\cdot}H_2O$ were dissolved in distilled water and then the obtained solution was transferred to hydrothermal vessel for the reaction at 140 °C for 12 h. After the reaction, the obtained powders were separated by centrifugation, washed thoroughly with distilled water, and dried overnight at 50 °C in oven. Several Ru contents of x = 0, 0.05, 0.1, 0.15, and 0.2 were employed for the synthesis of α-$Mn_{1-x}Ru_xO_2$ nanowires and the resulting materials are denoted as **MR0**, **MR05**, **MR10**, **MR15**, and **MR20**, respectively.

2.2. Characterization

The crystal structures of the present materials were probed with powder X-ray diffraction (XRD) (Rigaku D/Max-2000/PC, Ni-filtered Cu Kα radiation, λ = 1.5418 Å, 25 °C). The morphologies of the α-$Mn_{1-x}Ru_xO_2$ materials were monitored with field emission-scanning electron microscopy (FE-SEM) analysis (Jeol JSM-6700F). The transmission electron microscopy (TEM) images and energy dispersive spectrometry (EDS) − elemental maps were collected with a Jeol JEM-2100F microscope to probe the crystal shapes and elemental distributions of the present materials, respectively. The electronic configurations and local structures of Mn and Ru ions in the present materials were investigated using X-ray absorption near edge structure (XANES) and extended X-ray absorption fine structure (EXAFS) analysis at Mn K-edge and Ru K-edge at beam line 10C in the Pohang Accelerator Laboratory (PAL, Pohang, Korea). All the present XANES/EXAFS spectra were calibrated by measuring the spectrum of Mn or Ru element. X-ray photoelectron spectroscopy (XPS) data were collected by XPS machine (Thermo VG, UK, Al Kα). The energy calibration was done with a reference to adventitious C 1s XPS peak (BE = 284.8 eV). Micro-Raman spectra were measured to study the chemical bonding nature of manganese oxide (Horiba Jobin Yvon LabRam Aramis). An Ar-ion laser (λ = 514 nm) was used as the excitation source. N_2 adsorption − desorption isotherms were collected at 77 K using a Micromeritics ASAP 2020 analyzer.

2.3. Electrochemical measurement

The electrochemical measurements for both OER and ORR processes were carried out using a standard three electrode electrochemical cell at room temperature. A glassy carbon electrode (3 mm in diameter), a Pt wire, and a saturated calomel electrode (SCE) were employed as working, counter, and reference electrodes, respectively. 0.1 M KOH solution was used as an electrolyte. The OER and ORR polarization curves were measured by employing a RRDE-3A (ALS Co.) as a rotator. The homogeneous electrocatalyst ink was prepared as follows: 5.0 mg of electrocatalyst, 5.0 mg of carbon black (Vulcan-XC72R), and 25 μL of 5wt% Nafion solution were dispersed in 5.0 mL of mixed solvent of isopropanol and Milli-Q water (1/4, vol/vol), followed by high speed sonication for 1 h. To measure the electrocatalytic activity, 10 μL of ink (electrocatalyst loading of 0.14 mg cm^{-2}) was dropped on a glassy carbon electrode. The electrolyte was purged with O_2 gas for 30 min before the measurement. The electrochemical activities of OER and ORR were determined using linear sweep voltammetry (LSV) with a scan rate of 5 mV s^{-1} and a rotating speed of 1600 rpm. The potentials were converted to reversible hydrogen electrode (RHE) scale with following equation: E(RHE) = E(SCE) + 1.012 V. The electron transfer number in the ORR process could be calculated from the slope of Koutecky − Levich (K − L) plots [21]. The electrochemical impedance spectroscopy (EIS) data were collected with IVIUM analyzer in the frequency range of 0.1 − 100000 Hz at 1.65 V (V vs RHE). The electron paramagnetic resonance (EPR) spectra were measured by Bruker EMX/Plus spectrometer equipped with a dual mode cavity (ER4116DM) in KBSI, Seoul, Korea. EPR data were measured with parallel mode (9.4 GHz), modulation amplitude 10 G, modulation frequency 100 kHz and microwave power of 5.0 mW at 5 K. The electrocatalyst ink loaded on FTO glass (1.5 cm by 2.5 cm) was transferred to the EPR tube with mixed solution of 180 μL of 20 mM $Na_4P_2O_7$ solution and 20 μL glycerol right after the electrochemical reaction, and then frozen immediately by liquid nitrogen to avoid the decay of Mn^{3+} ions. Since the pyrophosphate has a strong tendency to ligate with Mn^{3+} species [22], this pyrophosphate solution was used to capture unstable Mn^{3+} ions via the formation of metal − ligand complex for the facilitated sensing of this transient species by EPR technique. A small amount of glycerol was added as a cryoprotectant to prevent a significant volume change of solution and the resulting shattering of sample tube during the freezing of the sample solution. More importantly, the high crystallity of ice can interrupt the crystal system of catalyst material, leading to the significant alteration of the chemical characterestics (e.g. ionic strength) of sample solution and the resulting modification of EPR spectra. Thus, the use of glycerol cryoprotectant is indispensable for collecting the well-defined EPR spectra through the prevention of highly-crystalline ice formation [22–24]. Before measurements, all the materials applied with a constant potential of 1.65 V (V vs RHE) for 30 min.

3. Results and discussion

3.1. Powder XRD Analysis

Fig. 1a presents the powder XRD patterns of Ru-substituted α-$Mn_{1-x}Ru_xO_2$ materials. Regardless of Ru substitution rate, all the present materials display typical Bragg reflections of α-MnO_2 phase without any impurity peaks, indicating the formation of single-phase Ru-substituted α-$Mn_{1-x}Ru_xO_2$ materials. The complete Ru substitution for α-MnO_2 material is further confirmed by Rietveld refinement, see Fig. 1b and Table S1 of Supporting Information. All the XRD peaks of the most heavily Ru-substituted **MR20** material are well reproduced with Ru-substituted α-MnO_2 structure, confirming the synthesis of single-phase α-$Mn_{1-x}Ru_xO_2$ material. As listed in Table 1, the unit cell volume becomes gradually larger with increasing the Ru substitution

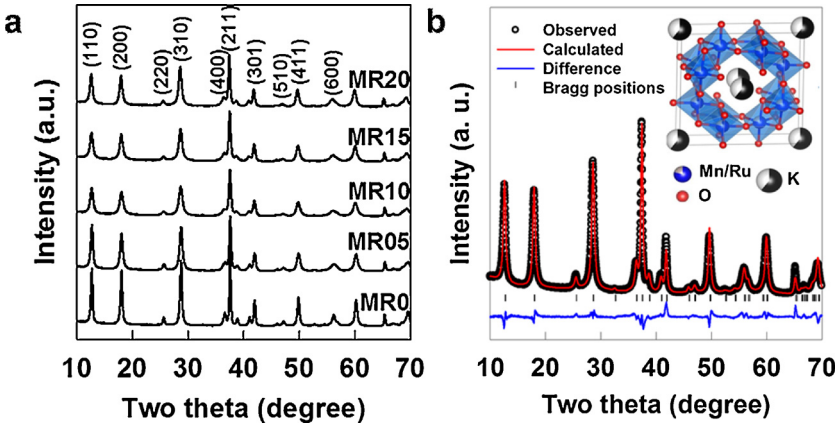

Fig. 1. (a) Powder XRD patterns of the Ru-substituted α-$Mn_{1-x}Ru_xO_2$ 1D nanowires and (b) the result of Rietveld refinement of **MR20** and (inset) its refined crystal structure.

Table 1
Lattice parameters and unit cell volumes of the Ru-substituted α-$Mn_{1-x}Ru_xO_2$ 1D nanowires.

Sample	*a* (Å)	*c* (Å)	Unit cell volume (Å^3)	RMS error
MR0	9.853	2.862	277.848	1.40E-04
MR05	9.858	2.861	278.032	8.91E-05
MR10	9.864	2.861	278.370	2.30E-04
MR15	9.866	2.862	278.581	1.34E-04
MR20	9.866	2.864	278.776	2.24E-04

rate. Judging from the relative sizes of Ru and Mn ions in octahedral site (Mn^{3+}: 0.72 Å, Mn^{4+}: 0.67 Å, Ru^{3+}: 0.82 Å, Ru^{4+}: 0.76 Å) [25], the expansion of unit cell volume confirms the replacement of Mn^{3+} and Mn^{4+} ions with bigger Ru^{3+} or Ru^{4+} ions. A slight expansion of unit cell volume caused by Ru substitution strongly suggests the incorporation of smaller Ru^{4+} ion rather than larger Ru^{3+} ion. Considering the fact that too big size difference between Mn and Ru would destabilize the Ru-substituted α-$Mn_{1-x}Ru_xO_2$ lattice, tetravalent oxidation state is supposed to be more feasible valence state for substituent Ru ion than trivalent one. In fact, the tetravalent Ru^{4+} oxidation state of substituted Ru ion is confirmed by Ru 3p XPS spectra (Fig. S1 of Supporting Information). All the α-$Mn_{1-x}Ru_xO_2$ 1D nanowires show two peaks at 463 and 485 eV, which are assigned as $3p_{3/2}$ and $3p_{1/2}$ peaks of Ru^{4+} species, respectively.

3.2. EXAFS and Micro-Raman Spectroscopic Analyses

The local structural evolution of the α-$Mn_{1-x}Ru_xO_2$ nanowire upon the Ru substitution is investigated with EXAFS and micro-Raman spectroscopies due to their sensitivity to the local symmetry of metal ions [26]. Figs. 2a and 2b present the Fourier transformed (FT) EXAFS spectra of the α-$Mn_{1-x}Ru_xO_2$ nanowires at Mn K- and Ru K-edges, respectively. In the Mn K- and Ru K-edges, all the present α-$Mn_{1-x}Ru_xO_2$ nanowires commonly display three intense FT peaks at ~1.5, ~2.6, and ~3.1 Å, which correspond to (Mn/Ru − O), edge-shared (Mn/Ru − Mn/Ru), and corner-shared (Mn/Ru − Mn/Ru) shells, respectively. This FT feature is typical of α-MnO_2 structure [27]. The observation of identical FT features in Mn K-edge and Ru K-edge spectra provides strong evidence for the co-existence of Mn and Ru ions in the same octahedral site of α-MnO_2 structure composed of edge-shared and corner-shared (Mn,Ru)O_6 octahedra. The complete substitution of Ru ion into the α-MnO_2 lattice is cross-confirmed by the remarkable difference in the Ru K-edge EXAFS oscillations and FT spectra of α-$Mn_{1-x}Ru_xO_2$ and reference RuO_2 (Fig. S2 of Supporting Information and Fig. 2b). Of prime importance is that the FT peak at ~1.5 Å corresponding to (Mn − O) shell shows a distinct depression with increasing the Ru content, see the right panel of Fig. 2a. Since the tetragonal deformation of MnO_6 octahedra leads to the depression of the FT peak of (Mn − O) shell due to the splitting of (Mn − O) bond distances [28], the observed decrease of the FT intensity upon the Ru substitution can be regarded as clear evidence for the enhanced tetragonal distortion of MnO_6 octahedra.

Micro-Raman spectra of the present α-$Mn_{1-x}Ru_xO_2$ materials are plotted in Fig. 2c. Regardless of Ru content, all the present materials show typical Raman spectral features of α-MnO_2 phase [29], confirming the maintenance of the original crystal structure of manganese oxide. As can be seen clearly from Fig. 2d, the substitution of Mn with Ru results in the depression of main peak at A_{1g} phonon line of MnO_6 octahedra, which is ascribable to the decrease of the concentration of (Mn − O) bonds with the increase of Ru content. Additionally, this peak shows distinct red-shift with the increase of Ru content, reflecting the weakening of (Mn − O) bond as well as the decrease of average Mn oxidation state. This is in good agreement with the Mn K-edge EXAFS result showing the enhanced tetragonal distortion of MnO_6 octahedra upon the Ru substitution. Since Ru has a higher electronegativity than Mn [19], the (Ru^{4+} − O) bond is supposed to be more covalent than the (Mn^{4+} − O) bond. As illustrated in Fig. 2e, the incorporation of more covalent (Ru − O) bond gives rise to the weakening and elongation of neighboring axial (Mn − O) bond via the bond competition, which is responsible for the observed enhancement of tetragonal distortion of MnO_6 octahedra and the red-shift of the A_{1g} Raman peak caused by the Ru substitution. The resulting weakening of neighboring (Mn − O) bond upon the Ru substitution is effective in stabilizing Jahn-Teller active Mn^{3+} species.

3.3. XPS and XANES Analyses

The effects of Ru substitution on the Mn oxidation states of surface and bulk Mn species are investigated with surface-sensitive XPS and bulk-sensitive XANES techniques, respectively [26]. Fig. 3a represents the Mn $2p_{3/2}$ XPS data of the present α-$Mn_{1-x}Ru_xO_2$ materials with the results of peak convolution analysis. For all the present spectra, the observed Mn $2p_{3/2}$ peak can be well-reproduced with three component peaks corresponding to the Mn^{3+}, Mn^{4+}, and satellite. As listed in Table S2 of Supporting Information, the relative concentration of Mn^{3+} species becomes greater with increasing the Ru substitution rate, indicating the formation of surface Mn^{3+} species upon the incorporation of Ru^{4+} ions. Conversely, as shown in the Mn K-edge XANES spectra of Fig. 3b and c, the edge energies of the α-$Mn_{1-x}Ru_xO_2$ materials and the intensity ratio of P'/P are identical to one another, which are higher than that of reference Mn_2O_3 but lower than that of reference λ-MnO_2, indicating the mixed Mn^{3+}/Mn^{4+} oxidation state of these materials

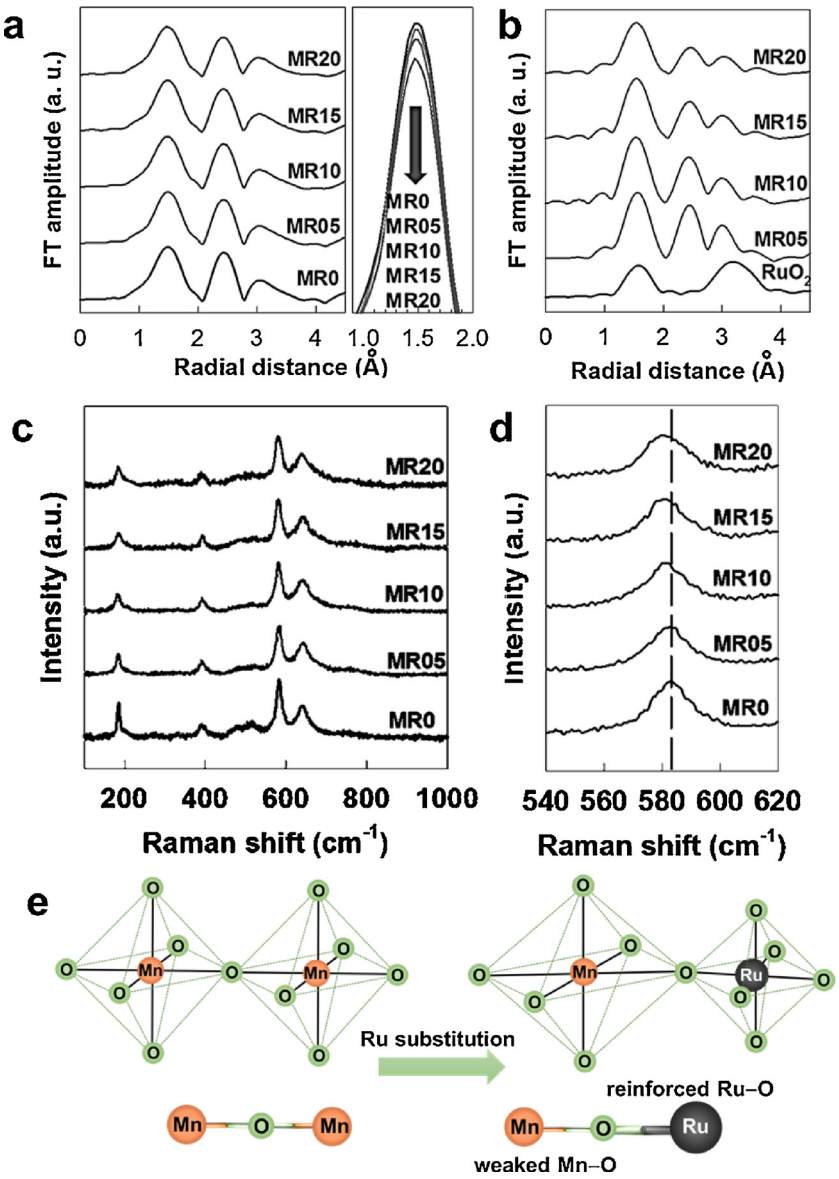

Fig. 2. The FT data of EXAFS spectra at (a) Mn K-edge and (b) Ru K-edge, and (c) micro-Raman spectra and (d) their expanded spectra for the Ru-substituted α-$Mn_{1-x}Ru_xO_2$ 1D nanowires and RuO_2 material, and (e) schematic model of the evolution of neighboring (Mn − O) bonds upon the incorporation of highly covalent (Ru^{4+} − O) bond into α-MnO_2 lattice.

and negligible change of Mn valency in the bulk state [30]. This XANES result is in stark contrast to notable red-shift of XPS peaks after the Ru substitution. Taking into account the high sensitivities of XPS and XANES to surface and bulk species, respectively [26], the present result clearly demonstrates that the replacement of Mn with Ru gives rise the formation of Mn^{3+} ions mainly on the surface not in the bulk state. Since the Mn^{3+} ion is Jahn-Teller active, this ion can be stabilized in the tetragonally-distorted MnO_6 octahedral geometry. Because the surface Mn site has less saturated coordination environment and higher structural flexibility than does the bulk Mn site, the surface Mn site is more favorable for accommodating Jahn-Teller-active Mn^{3+} ions via the increase of tetragonal distortion, as supported by the previous reports [31,32]. As a result, the Ru substitution leads to the preferential formation of Mn^{3+} ions on the surface. As many articles insisted, these Mn^{3+} species with the electron configuration of $t_{2g}^3e_g^1$ can act as a critical role in the electrocatalytic activity of manganese oxide for OER and ORR processes [33,34]. The presence of one electron in anti-bonding e_g orbital provides an appropriate strength of interaction with oxygen species, which is beneficial for promoting both OER and ORR processes [34]. Since the electrocatalyst reaction occurs on the surface of α-MnO_2 material, the preferential formation of Mn^{3+} species on the surface is more advantageous in improving the electrocatalytic activity of the present material by the Ru substitution.

The tetravalent Ru oxidation state of the present material is also confirmed by Ru K-edge XANES analysis. As presented in Fig. 3d, all the Ru-substituted α-$Mn_{1-x}Ru_xO_2$ 1D nanowires display almost the same Ru K-edge energies as that of the reference RuO_2, indicating the tetravalent Ru^{4+} oxidation state in the present materials [35]. This is in good agreement with the Ru 3p XPS result (Fig. S1 of Supporting Information). The variation of Ru content does not induce any significant spectral change of Ru K-edge XANES spectra, clearly demonstrating the negligible change of Ru local structure over the present Ru substitution range. Summarizing all the present XPS, XANES/EXAFS and micro-Raman results, the substitution of Ru^{4+} ion is quite effective in tailoring the chemical bonding nature, local crystal structure, and Mn valence state of α-MnO_2 material.

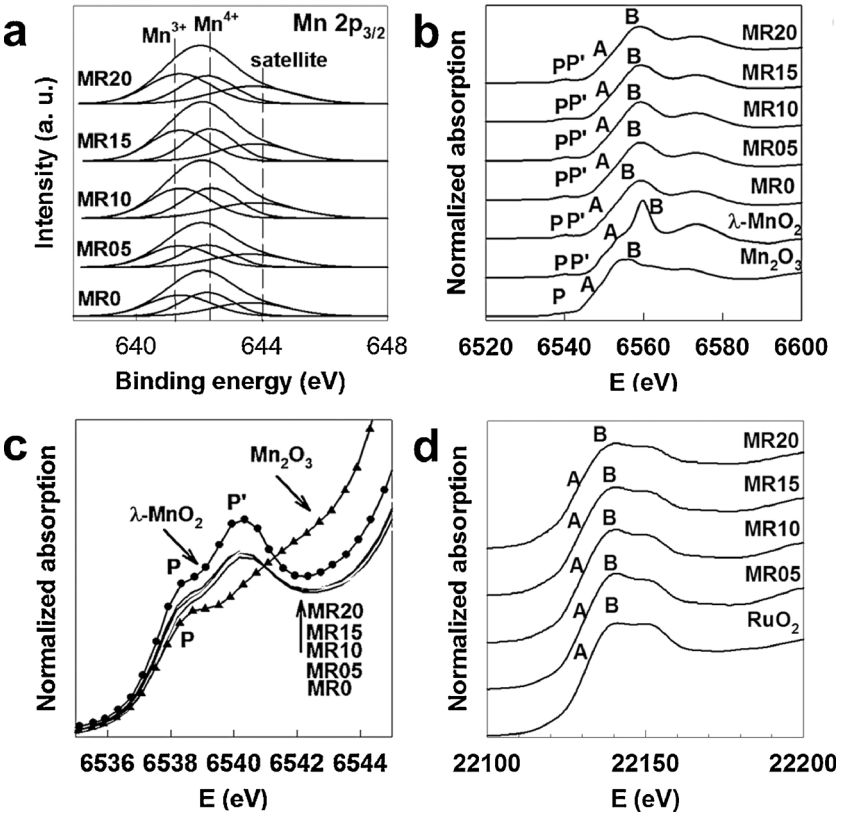

Fig. 3. (a) Mn 2p XPS, (b) Mn K-edge XANES spectra and (c) their expanded views of edge jump region, and (d) Ru K-edge XANES spectra of the Ru-substituted α-$Mn_{1-x}Ru_xO_2$ 1D nanowires and several references.

3.4. FE-SEM, TEM, and EDS – Elemental Mapping Analyses

The evolution of the crystal morphology of α-$Mn_{1-x}Ru_xO_2$ upon the Ru substitution is examined with FE-SEM and TEM analyses. As presented in Fig. 4a, regardless of Ru content, all the present materials exhibit highly anisotropic 1D nanowire morphology, confirming the maintenance of 1D crystal morphology upon Ru substitution. Low magnification FE-SEM data clearly demonstrate the uniform formation of 1D nanowire. As the Ru content increases, the length of 1D nanowire becomes shorter. This observation is attributable to the mismatch of the ionic sizes of manganese and ruthenium ions, leading to the frustration of the crystal growth of 1D nanowire upon Ru substitution. As illustrated in Fig. 4b, the present TEM images of α-$Mn_{1-x}Ru_xO_2$ nanowires also provide strong evidence for the shortening of 1D nanowire caused by the Ru substitution. The EDS – elemental mapping analysis confirms uniform replacement of Mn with Ru. As illustrated in Fig. 4c, the **MR20**

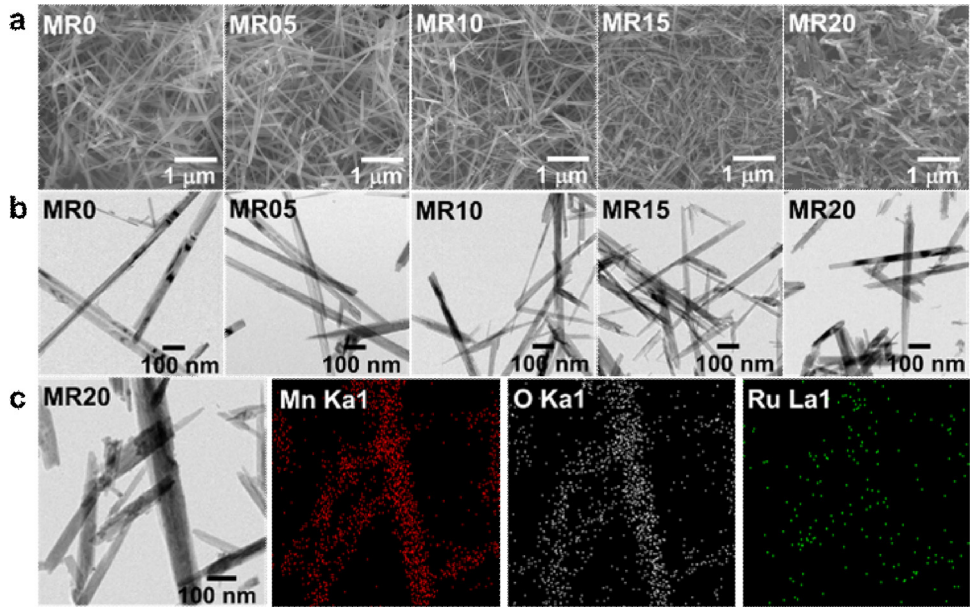

Fig. 4. (a) FE-SEM images, (b) TEM images, and (c) EDS – elemental maps of the Ru-substituted α-$Mn_{1-x}Ru_xO_2$ 1D nanowires.

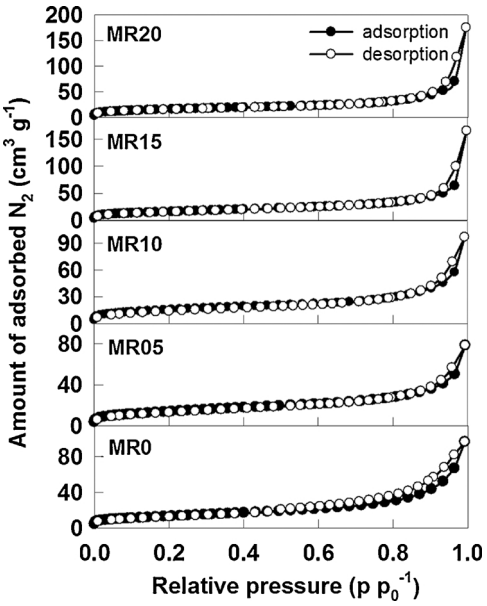

Fig. 5. N_2 adsorption – desorption isotherms of the Ru-substituted α-$Mn_{1-x}Ru_xO_2$ 1D nanowires.

material displays homogeneous distribution of Mn, Ru, and O elements in the entire region of the material including the surface and core of nanowires, clearly demonstrating the uniform replacement of Mn with Ru.

3.5. N_2 Adsorption – Desorption Isotherm Analysis

N_2 adsorption – desorption isotherm analysis is carried out to probe the effect of Ru substitution on the specific surface areas of α-$Mn_{1-x}Ru_xO_2$ nanowires. As plotted in Fig. 5, all the present materials show nearly identical isotherm behavior with weak hysteresis, classified as Brunauer – Deming – Deming – Teller (BDDT) type IV isotherm with H3-type hysteresis loop [36,37], showing the absence of distinct pores in the present materials. According to the calculation of specific surface area based on Brunauer – Emmett – Teller (BET) equation, the present Ru-substituted α-$Mn_{1-x}Ru_xO_2$ 1D nanowires possess expanded specific surface areas of 48 $m^2\ g^{-1}$ for **MR0**, 50 $m^2\ g^{-1}$ for **MR05**, 55 $m^2\ g^{-1}$ for **MR10**, 57 $m^2\ g^{-1}$ for **MR15**, and 56 $m^2\ g^{-1}$ for **MR20**, respectively. The incorporation of Ru ions leads to a slight increase of the specific surface area of manganese oxide nanowire, which is related to the decrease of aspect ratio upon Ru substitution, as evidenced by the FE-SEM and TEM results. Such an increase of the specific surface area of α-$Mn_{1-x}Ru_xO_2$ upon the Ru substitution is helpful for enhancing electrocatalytic activities of materials, since the OER and ORR processes occur mainly on the surface of catalyst [38–40]. In addition to the α-$Mn_{1-x}Ru_xO_2$ nanowires, the specific surface areas of the references Ir/C, Pt/C, and the physical mixture of α-MnO_2 and RuO_2 (mole ratio of 8:2) are also estimated with N_2 adsorption – desorption isotherm analysis. As plotted in Fig. S3 of Supporting Information, these reference materials possess specific surface area of 198 $m^2\ g^{-1}$ for 20wt% Ir/C, 179 $m^2\ g^{-1}$ for 20wt% Pt/C, and 22 $m^2\ g^{-1}$ for the physical mixture of α-MnO_2 and RuO_2.

3.6. Test of Electrocatalyst Activity for OER and ORR

The Ru-substituted α-$Mn_{1-x}Ru_xO_2$ nanowires are tested as electrocatalysts for OER, as compared with commercial 20wt% Ir/C electrocatalyst. As plotted in Fig. 6a, the Ru-free **MR0** material displays significant OER electrocatalytic activity, which is however much inferior to that of commercial 20wt% Ir/C. The partial substitution of Mn with Ru leads to the significant improvement of OER electrocatalytic activity with the increase of current density and the decrease of on-set potential, clearly demonstrating the beneficial effect of substituted Ru ion on the OER activity of α-MnO_2. Among the Ru-substituted α-$Mn_{1-x}Ru_xO_2$ materials, the **MR20** material displays the best OER electrocatalyst performance with very low on-set potential which is almost the same as that of the commercial Ir/C. Of prime importance is that the **MR20** material shows even greater current density than does the Ir/C electrocatalyst, although the specific surface area of the former is much smaller than that of the latter (Fig. 5 and Fig. S3 of Supporting Information). This highlights the unique advantage of Ru substitution in remarkably improving the OER and ORR electrocatalytic activities of manganese oxide.

To verify the merit of Ru substitution in improving the OER performance of α-MnO_2, the electrocatalytic activity of the physical mixture of α-MnO_2 and RuO_2 (mole ratio of 8:2) for OER is also examined. As can be seen clearly from Fig. 6b, the physical mixture shows better OER electrocatalytic activity than the unsubstituted **MR0**, which is attributable to the provision of the highly OER electrocatalytically active Ru site in the RuO_2 component [41]. Even with the same Ru content, the physical mixture of α-MnO_2 and RuO_2 is less active as an OER catalyst compared with **MR20**. The difference in overpotential is greater for the couple of **MR20** and the physical mixture than that of the physical mixture and **MR0**, underscoring that, in comparison with the provision of electrocatalytically active Ru site occurred by physical mixing, the increase of Mn^{3+} content by the Ru substitution can make a greater contribution to the improvement of the OER activity of α-$Mn_{1-x}Ru_xO_2$ materials upon the Ru substitution. In addition to the increase of Mn^{3+} content, the increase of surface area upon the Ru substitution can make a significant contribution to the improvement of OER activity [42]. However, even with slight increase of surface area (i.e. ~8 – 9 $m^2\ g^{-1}$), the Ru substitution induces a remarkable lowering of overpotential (i.e. −120 mV at 10 mA cm^{-2}), strongly suggesting a minor contribution of surface expansion to the notable enhancement of OER activity upon the Ru substitution.

The Tafel slopes are calculated to examine the electrocatalytic kinetic of OER process by the present materials. As presented in Fig. 6c, the Tafel value is determined to be 106 mV dec^{-1} for **MR0**, 103 mV dec^{-1} for **MR05**, 100 mV dec^{-1} for **MR10**, 94 mV dec^{-1} for **MR15**, 86 mV dec^{-1} for **MR20**, 101 mV dec^{-1} for the physical mixture of α-MnO_2 and RuO_2, and 85 mV dec^{-1} for commercial Ir/C, respectively. Since a smaller value of Tafel slope implies a better OER kinetics [43], this result strongly suggests the significant enhancement of OER reaction kinetics upon the Ru substitution. A much smaller Tafel slope of **MR20** than the physical mixture of α-MnO_2 and RuO_2 strongly suggests that the improvement of OER kinetics upon the Ru substitution is mainly attributable to the control of Mn valency rather than to the provision of Ru sites.

The dependence of the charge-transfer behavior of α-$Mn_{1-x}Ru_xO_2$ nanowires on the Ru content is also examined with EIS. As shown in Fig. 6d, at the applied potential of 1.65 V (vs RHE), all the present α-$Mn_{1-x}Ru_xO_2$ nanowires demonstrate notably reduced diameters of the semicircle than does the unsubstituted α-MnO_2, reflecting the decrease of charge transfer resistance (R_{ct}) upon the Ru substitution [44]. According to fitting analysis for the EIS data with equivalent circuit (Fig. 6e), all the Ru-substituted α-$Mn_{1-x}Ru_xO_2$ nanowires show smaller R_{ct} values of 883.7, 750.7, 211.0, and 102.6 Ω for **MR05**, **MR10**, **MR15**, and **MR20**, respectively, compared with that of **MR0** (2978 Ω), confirming the enhancement of the charge-transfer kinetics of α-$Mn_{1-x}Ru_xO_2$ nanowire by the Ru substitution. The validities of the present fits are verified by small values of χ^2 (0.00076 – 0.0025). As plotted in Fig. S4 of Supporting Information, the physical mixture of α-MnO_2 and RuO_2 (mole ratio of 8:2) shows a much larger diameter of the semicircle than does **MR20**, indicating that, in comparison with the addition of conductive RuO_2 component, the modification of the Mn valency and electronic structure of α-MnO_2 upon the Ru substitution is

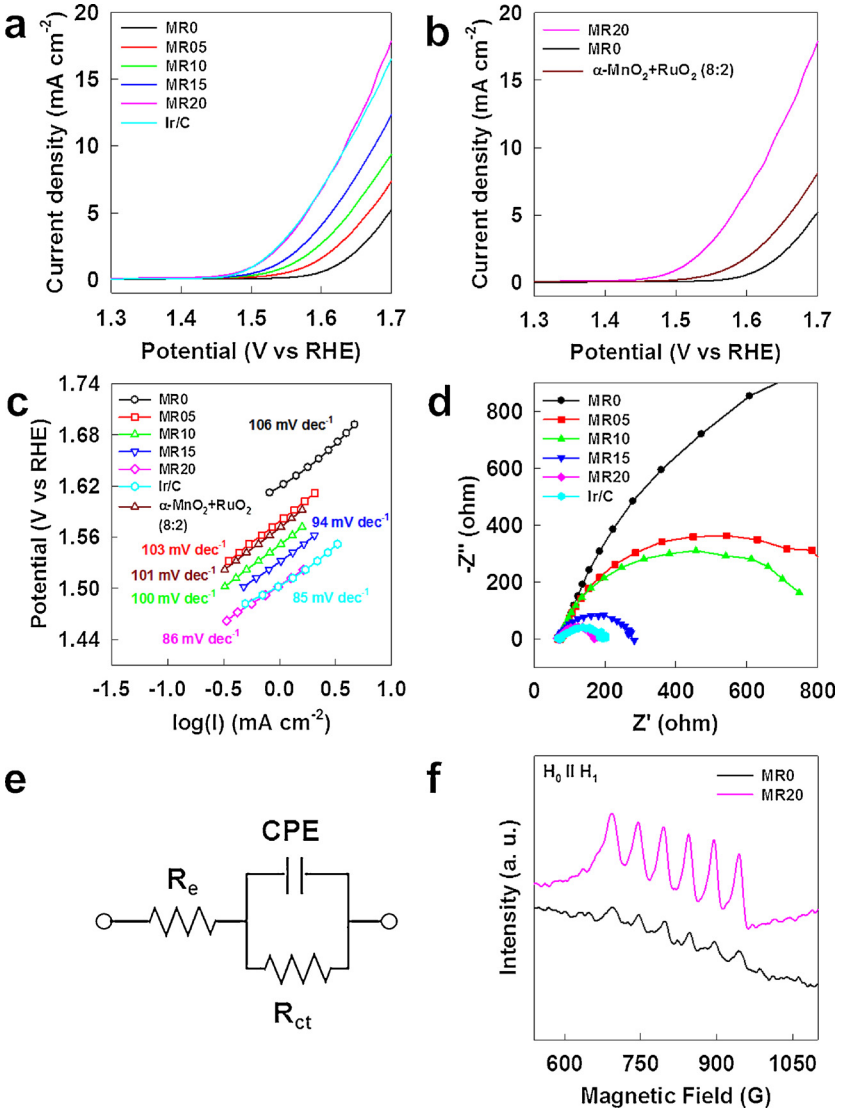

Fig. 6. (a, b) OER polarization curves, (c) Tafel plots, (d) EIS data, (e) equivalent circuit for EIS analysis and (f) X-band EPR spectra (parallel mode) for the Ru-substituted α-$Mn_{1-x}Ru_xO_2$ 1D nanowires and the physical mixture of α-MnO_2 and RuO_2 (mole ratio of 8:2). In (e), the R_e, R_{ct}, and CPE represent electrolyte resistance, charge transfer resistance, and constant phase element, respectively.

mainly responsible for the observed improvement of charge-transfer kinetics.

To better understand the Ru substitution effect on the OER electrocatalytic process, the EPR measurements are carried out to probe the formation of Mn^{3+} ion playing an important role in the electrocatalytic activity of manganese oxide. As presented in Fig. 6f, the X-band parallel mode EPR spectrum of **MR20** subjected to the OER electrocatalytic experiments displays six ^{55}Mn hyperfine splitting (I = 5/2) peaks around 800 G (g_{eff} ~ 8) corresponding to Mn^{3+} ions (S = 2) [45]. This result underscores the involvement of Mn^{3+} ions in the electrocatalytic processes. The Mn^{3+} signal of **MR20** is much stronger than that of **MR0**, demonstrating that **MR20** has higher concentration of Mn^{3+} species during the OER process. This result confirms the stabilization of unstable Mn^{3+} species by the Ru substitution.

Recently it is reported that the OER application of metal oxide electrocatalyst induces the self-reconstruction of its surface with the formation of a highly OER active amorphous oxy(hydroxide) layer [46,47]. Similarly, the present α-MnO_2 nanowire would experience the formation of manganese oxy(hydroxide) phase during the OER process. The possible surface reconstruction of α-$Mn_{1-x}Ru_xO_2$ with the formation of manganese oxy(hydroxide) layer is examined using *in-situ* micro-Raman analysis during the OER process. As shown in Fig. S5 of Supporting Information, both the **MR0** and **MR20** materials commonly show neither notable spectral modification nor the appearance of manganese oxy(hydroxide)-related Raman peaks under the application of electrical potentials of 0, 1.5, 1.6, 1.7, and 1.8 V (V vs RHE), strongly suggesting no significant reconstruction of α-$Mn_{1-x}Ru_xO_2$ structure and no formation of manganese oxy(hydroxide) layer during the OER process. Even with these Raman results, there still remains a possibility for the formation of very small amount of amorphous manganese oxy (hydroxide) layer below the detection limit of micro-Raman spectroscopy. However, even if the electrocatalytic activity of α-$Mn_{1-x}Ru_xO_2$ material relies on the formation of manganese oxy(hydroxide) layer, the control of chemical bonding nature upon the Ru substitution would be still responsible for the improved electrocatalyst performance of Ru-substituted α-$Mn_{1-x}Ru_xO_2$ materials. Since the manganese oxy(hydroxide) has a formula of MnO(OH) with trivalent Mn^{3+} oxidation state but there is no manganese oxy(hydroxide) with tetravalent Mn^{4+} oxidation state, the stabilization of Mn^{3+} species by the Ru substitution is also effective in promoting the surface reconstruction of α-MnO_2 nanowire with trivalent manganese oxy(hydroxide) layer. This promoted surface reconstruction would contribute to the enhancement of the OER

activity upon the Ru substitution. In fact, the remarkably enhanced Mn^{3+}-related EPR peaks for the Ru-substituted **MR20** during the OER process can be regarded as convincing evidence for the promoted formation of trivalent manganese oxy(hydroxide) layer caused by the Ru substitution (Fig. 6f). This result clearly demonstrates the beneficial effect of controlling the bond characteristics on the electrocatalytic activity of α-MnO_2 via the promoted formation of metal oxy(hydroxide) layer.

The enhancement of the electrocatalytic stability of α-MnO_2 nanowire upon Ru substitution is further evidenced by the long-term stability test of OER activity, as presented in Fig. S6 of Supporting Information. At a constant current of 5 mA cm^{-2}, both the Ru-substituted **MR15** and **MR20** materials can retain initial potential upto 10,000 s, whereas the unsubstituted **MR0** material suffers from a fast decay of OER activity, underscoring the significant improvement of electrocatalytic durability upon the Ru substitution. The improved durabilities of Ru-substituted **MR15** and **MR20** materials are attributable to the enhancement of electrical conductivity upon Ru substitution, which depresses the thermally-induced structural deterioration of poorly-conductive α-MnO_2 material during the repeated application of electric potential [48]. Also, an increase of the active sites of α-MnO_2 upon Ru substitution makes additional contribution to the enhanced durability of the Ru-substituted materials, since the increase of active sites can improve the durability of electrocatalyst [49].

To verify the role of Ru-substituted α-$Mn_{1-x}Ru_xO_2$ nanowires as bifunctional electrocatalysts, the ORR electrocatalytic activities of these materials are also tested by LSV measurement, as compared with that of commercial 20wt% Pt/C. As presented in Fig. 7a, the Ru-substituted α-$Mn_{1-x}Ru_xO_2$ materials exhibit higher ORR activity than does the Ru-free **MR0**, indicating the usefulness of Ru substitution in improving the ORR activity of α-MnO_2 nanowire. Among the materials under investigation, the **MR15** shows the best ORR performance with the greatest current density and the most positive onset potential. As a result of a significant positive shift of half-wave potential by > 150 mV upon the Ru substitution, the half-wave potential of **MR15** becomes nearly comparable to that of commercial Pt/C electrocatalyst, although the **MR15** has much smaller specific surface area than does Pt/C (Fig. 5 and Fig. S3 of Supporting Information).

Like the OER tests, the ORR activity of the physical mixture of α-MnO_2 and RuO_2 (mole ratio of 8:2) is also compared with those of **MR0** and **MR20** to verify the unique advantage of Ru substitution. As plotted in Fig. 7b, the physical mixing of **MR0** (i.e. α-MnO_2) with RuO_2 induces a slight decrease of overpotential for ORR, which is attributable to the addition of electrocatalytically active and conductive RuO_2 component [50]. Of prime importance is that, even with the same Ru content, the ORR electrocatalytic activity of **MR20** is much higher than that of the physical mixture of α-MnO_2 and RuO_2 (8:2), confirming that the improved ORR performances of α-$Mn_{1-x}Ru_xO_2$ materials originate mainly from the controlled Mn valency by Ru substitution, rather from the simple provision of electrocatalytically active Ru site. The evolution of the ORR kinetics of α-MnO_2 upon the Ru substitution is studied by calculating the Tafel slopes of α-$Mn_{1-x}Ru_xO_2$ materials. As shown in Fig. 7c, the Ru-substituted materials show smaller Tafel slopes of 87, 86, 60, and 61 mV dec^{-1} for **MR05**, **MR10**, **MR15**, and **MR20**, respectively, as compared with that of **MR0** (155 mV dec^{-1}). Even with the same Ru mole ratio, the **MR20** exhibits a smaller Tafel slope than the physical mixture of α-MnO_2 and RuO_2 (71 mV dec^{-1}), confirming the significant merit of Ru substitution in increasing the ORR activity of α-MnO_2. As plotted in Fig. 7d, the K−L plots of the Ru-substituted α-$Mn_{1-x}Ru_xO_2$ nanowires are constructed based on LSV curves measured with different rotating speeds (Fig. S7 of Supporting Information) to gain additional insight for the ORR process of these materials. From the slope of the K−L plots, the electron transfer numbers (n) of the present materials are estimated as 3.55, 3.45, 3.58, 3.86, and 3.83 for **MR0**, **MR05**, **MR10**, **MR15**, and **MR20**, respectively. As the Ru content increases, the electron transfer number becomes closer to the desirable value of four ($O_2 + 2H_2O + 4e^- \rightarrow 4OH^-$). This result strongly suggests that the Ru substitution is quite effective in improving the

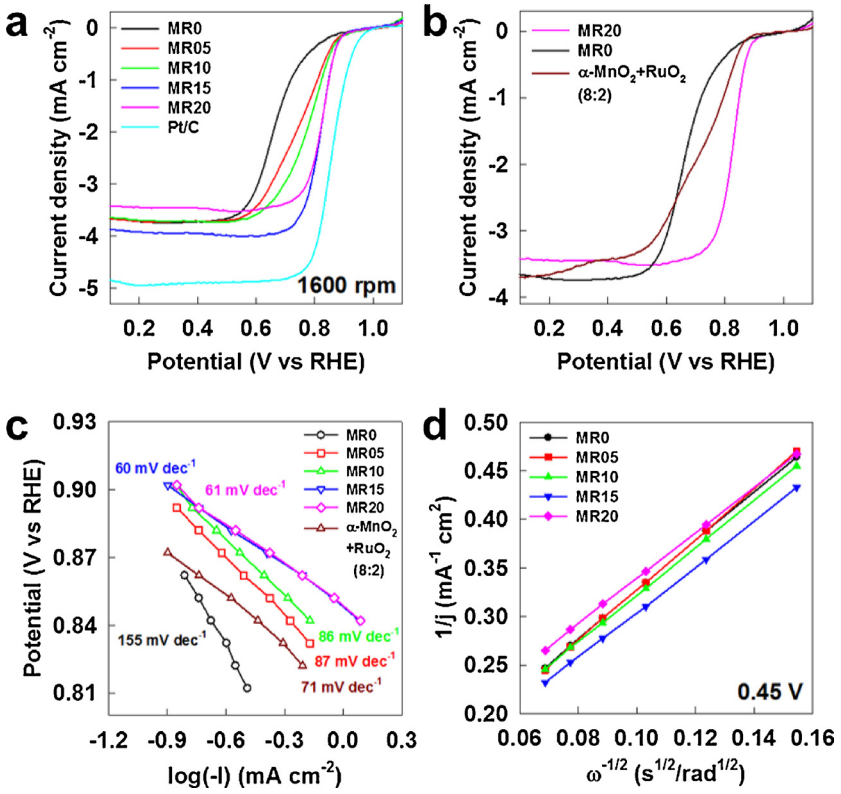

Fig. 7. (a, b) ORR polarization curves, (c) Tafel plots, and (d) K−L plots of the electrocatalysts at the potential of 0.45 V (vs RHE) for the Ru-substituted α-$Mn_{1-x}Ru_xO_2$ 1D nanowires.

selectivity of α-MnO_2 to four-electron ORR pathway.

Summarizing all the experimental findings presented here, the Ru substitution for the α-MnO_2 nanowire is highly effective in exploring high performance bifunctional electrocatalysts active for both OER and ORR. As found from the XPS, EXAFS, EPR, and micro-Raman results, the introduction of highly covalent ($Ru^{4+}-O$) bond causes the weakening and elongation of neighboring axial ($Mn-O$) bond, leading to the stabilization of Jahn-Teller active Mn^{3+} ion, as illustrated in Fig. 2e. Since both the MnO_2-assisted OER and ORR processes evolve the reversible redox transitions of $Mn^{2+} \leftrightarrow Mn^{3+} \leftrightarrow Mn^{4+}$ [12], the stabilization of unstable Mn^{3+} species caused by the Ru substitution plays a critical role in optimizing the electrocatalytic activity of α-MnO_2. Also, the weakening of ($Mn-O$) bond distance upon the Ru substitution provides appropriate strength of interaction with O_2, which is advantageous for improving the electrocatalyst activity for OER and ORR [33,34]. In addition to the control of Mn valency upon the Ru substitution, the provision of electrocatalytic active Ru site would make additional contribution to the superior electrocatalytic activity of Ru-substituted α-$Mn_{1-x}Ru_xO_2$ material. However, the comparison of α-$Mn_{1-x}Ru_xO_2$ with the physical mixture of α-MnO_2 and RuO_2 clearly demonstrates that the stabilization of unstable Mn^{3+} species makes a greater contribution to the observed improvement of electrocatalytic activity upon Ru substitution compared with the provision of active Ru sites.

4. Conclusions

In this work, highly efficient bifunctional MnO_2-based electrocatalysts for both OER and ORR can be synthesized by controlling the bond covalency of ($Mn-O$) and Mn valence state via Ru substitution in terms of bond competition with ($Ru-O$). The replacement of Mn ion with more electronegative Ru ion weakens adjacent ($Mn-O$) bonds due to bond competition, enhancing the stability of Jahn-Teller active Mn^{3+} species, a crucial component for the electrocatalyst activity of manganese oxide. Although the Ru substitution also provide electrocatalyticaly active Ru sites for α-MnO_2 material, this effect makes a smaller contribution to the observed improvement of electrocatalytic activity upon the Ru substitution than does the stabilization of Mn^{3+} species caused by the tailoring of ($Mn-O$) bond covalency. Of prime importance is that the electrocatalytic activities of the Ru-substituted α-$Mn_{1-x}Ru_xO_2$ materials for both OER and ORR are superior to and/or compatible with those of commercial noble metal electrocatalysts of Ir/C and Pt/C. Although several Co and Ni-based oxides show promising electrocatalytic activity for both OER and ORR [51–53], the superior cost-effectiveness and environmental friendliness of manganese oxides over cobalt oxides and nickel oxides render α-$Mn_{1-x}Ru_xO_2$ one of the most cost-effective metal oxide-based electrocatalysts. Additionally, the price of Ru element is much cheaper by $\sim 10-30$ times than those of Pt and Ir ones, respectively [54]. Thus, the present α-$Mn_{1-x}Ru_xO_2$ nanowires are promising alternatives to commercial Ir/C and Pt/C as bifunctional electrocatalysts for both OER and ORR. From the viewpoint of mass-production, the easiness and scalability of the present one-pot hydrothermal synthesis method enable to prepare more than tens of gram of the α-$Mn_{1-x}Ru_xO_2$ electrocatalysts in a single batch. This simple synthesis process can be easily scaled up to plant-level, enabling to produce kilograms and/or tons of the materials. In conclusion, the present study clearly demonstrates that the one-pot hydrothermal synthesis of cation-substituted MnO_2 nanowires can provide a scalable and cost-effective synthetic route to high performance MnO_2-based bifunctional electrocatalysts for both OER and ORR. Our current project is the application of the present α-$Mn_{1-x}Ru_xO_2$ materials as electrodes for metal – air batteries.

Acknowledgments

[1] These authors contributed equally to this work. This work was supported by the National Research Foundation of Korea (NRF) grant funded by the Korea government (MSIP) (No. NRF-2017R1A2A1A17069463) and by the Korea government (MSIT) (No. NRF-2017R1A5A1015365). The experiments at PAL were supported in part by MOST and POSTECH.

Appendix A. Supplementary data

Supplementary material related to this article can be found, in the online version, at doi:https://doi.org/10.1016/j.apcatb.2018.05.010.

References

[1] S.I. Shin, A. Go, I.Y. Kim, J.M. Lee, Y. Lee, S.-J. Hwang, A Beneficial Role of Exfoliated Layered Metal Oxide Nanosheets in Optimizing the Electrocatalytic Activity and Pore Structure of Pt-reduced Graphene Oxide Nanocomposites, Energy Environ. Sci. 6 (2013) 608–617.
[2] Z. Chen, A. Yu, D. Higgins, H. Li, H. Wang, Z. Chen, Highly Active and Durable Core-corona Structured Bifunctional Catalyst for Rechargeable Metal – Air Battery Application, Nano Lett. 12 (2012) 1946–1952.
[3] T. Zhan, X. Liu, S. Lu, W. Hou, Nitrogen Doped NiFe Layered Double Hydroxide/Reduced Graphene Oxide Mesoporous Nanosphere as an Effective Bifunctional Electrocatalyst for Oxygen Reduction and Evolution Reactions, Appl. Catal., B 205 (2017) 551–558.
[4] X. Jin, J. Lim, N.-S. Lee, S.-J. Hwang, A Powerful Role of Exfoliated Metal Oxide 2D Nanosheets as Additives for Improving Electrocatalyst Functionality of Graphene, Electrochim. Acta 235 (2017) 720–729.
[5] M. Shao, Q. Chang, J.-P. Dodelet, R. Chenitz, Recent Advances in Electrocatalysts for Oxygen Reduction Reaction, Chem. Rev. 116 (2016) 3594–3657.
[6] G.-L. Tian, M.-Q. Zhao, D. Yu, X.-Y. Kong, J.-Q. Huang, Q. Zhang, F. Wei, Nitrogen-Doped Graphene/Carbon Nanotube Hybrids: In Situ Formation on Bifunctional Catalysts and Their Superior Electrocatalytic Activity for Oxygen Evolution/Reduction Reaction, Small 10 (2014) 2251–2259.
[7] S. Dresp, F. Luo, R. Schmack, S. Kühl, M. Gliech, P. Strasser, An Efficient Bifunctional Two-Component Catalyst for Oxygen Reduction and Oxygen Evolution in Reversible Fuel Cells, Electrolyzers and Rechargeable Air Electrodes, Energy Environ. Sci. 9 (2016) 2020–2024.
[8] S. Cai, Z. Meng, H. Tang, Y. Wang, P. Tsiakaras, 3D Co-N-doped Hollow Carbon Spheres as Excellent Bifunctional Electrocatalysts for Oxygen Reduction Reaction and Oxygen Evolution Reaction, Appl. Catal., B 217 (2017) 477–484.
[9] M.S. Burke, L.J. Enman, A.S. Batchellor, S. Zou, S.W. Boettcher, Oxygen Evolution Reaction Electrocatalysis on Transition Metal Oxides and (Oxy)hydroxides: Activity Trends and Design Principles, Chem. Mater. 27 (2015) 7549–7558.
[10] Y. Meng, W. Song, H. Huang, Z. Ren, S.-Y. Chen, S.L. Suib, Structure-Property Relationship of Bifunctional MnO_2 Nanostructures: Highly Efficient, Ultra-Stable Electrochemical Water Oxidation and Oxygen Reduction Reaction Catalysts Identified in Alkaline Media, J. Am. Chem. Soc. 136 (2014) 11452–11464.
[11] K. Selvakumar, S.M.S. Kumar, R. Thangamuthu, G. Kruthika, P. Murugan, Development of shape-engineered α-MnO_2 materials as Bi-Functional catalysts for oxygen evolution reaction and oxygen reduction reaction in alkaline medium, Int. J. Hydrogen Energy 39 (2014) 21024–21036.
[12] T. Takashima, K. Hashimoto, R. Nakamura, Inhibition of Charge Disproportionation of MnO_2 Electrocatalysts for Efficient Water Oxidation under Neutral Conditions, J. Am. Chem. Soc. 134 (2012) 18153–18156.
[13] P.F. Smith, B.J. Deibert, S. Kaushik, G. Gardner, S. Hwang, H. Wang, J.F. Al-Sharab, E. Garfunkel, L. Fabris, J. Li, G.C. Dismukes, Coordination Geometry and Oxidation State Requirements of Corner-Sharing MnO_6 Octahedra for Water Oxidation Catalysis: An Investigation of Manganite (γ-MnOOH), ACS Catal. 6 (2016) 2089–2099.
[14] I.M. Mosa, S. Biswas, A.M. El-Sawy, V. Botu, C. Guild, W. Song, R. Ramprasad, J.F. Rusling, S.L. Suib, Tunable Mesoporous Manganese Oxide for High Performance Oxygen Reduction and Evolution Reactions, J. Mater. Chem. A 4 (2016) 620–631.
[15] T.N. Lambert, J.A. Vigil, S.E. White, C.J. Delker, D.J. Davis, M. Kelly, M.T. Brumbach, M.A. Rodriguez, B.S. Swartzentruber, Understanding the Effects of Cationic Dopants on α-MnO_2 Oxygen Reduction Reaction Electrocatalysis, J. Phys. Chem. C 121 (2017) 2789–2797.
[16] D.J. Davis, T.N. Lambert, J.A. Vigil, M.A. Rodriguez, M.T. Brumbach, E.N. Coker, S.J. Limmer, Role of Cu-Ion Doping in Cu-α-MnO_2 Nanowire Electrocatalysts for the Oxygen Reduction Reaction, J. Phys. Chem. C 118 (2014) 17342–17350.
[17] K. Jin, J. Park, J. Lee, K.D. Yang, G.K. Pradhan, U. Sim, D. Jeong, H.L. Jang, S. Park, D. Kim, N.-E. Sung, S.H. Kim, S. Han, K.T. Nam, Hydrated Manganese(II) Phosphate ($Mn_3(PO_4)_2{\cdot}3H_2O$) as a Water Oxidation Catalyst, J. Am. Chem. Soc. 136 (2014) 7435–7443.
[18] S.G. Hur, D.H. Park, T.W. Kim, S.-J. Hwang, Evolution of the Chemical Bonding Nature of Ferroelectric Bismuth Titanate upon Cation Substitution, Appl. Phys. Lett. 85 (2004) 4130–4132.
[19] K.S. Lackner, G. Zweig, Introduction to the Chemistry of Fractionally Charged Atoms: Electronegativity, Phys. Rev. D. 28 (1983) 1671–1691.
[20] S.H. Lee, T.W. Kim, D.H. Park, J.-H. Choy, S.-J. Hwang, N. Jiang, S.E. Park, Y.H. Lee, Single-Step Synthesis, Characterization, and Application of Nanostructured $K_xMn_{1-y}Co_yO_{2-\delta}$ with Controllable Chemical Compositions and

Crystal Structures, Chem. Mater. 19 (2007) 5010–5017.
[21] H. Hu, L. Han, M. Yu, Z. Wang, X.W. Lou, Metal-Organic-Framework-Engaged Formation of Co Nanoparticle-Embedded Carbon@Co_9S_8 Double-Shelled Nanocages for Efficient Oxygen Reduction, Energy Environ. Sci. 9 (2016) 107–111.
[22] J.K. Klewicki, J.J. Morgan, Kinetic Behavior of Mn(III) Complexes of Pyrophosphate, EDTA, and Citrate, Environ. Sci. Technol. 32 (1998) 2916–2922.
[23] K. Jin, A. Chu, J. Park, D. Jeong, S.E. Jerng, U. Sim, H.-Y. Jeong, C.W. Lee, Y.-S. Park, K.D. Yang, G.K. Pradhan, D. Kim, N.-E. Sung, S.H. Kim, K.T. Nam, Partially Oxidized Sub-10 nm MnO Nanocrystals with High Activity for Water Oxidation Catalysis, Sci. Rep. 5 (2015) 10279.
[24] M. Brustolon, E. Giamello, Electron Paramagnetic Resonance: A Practitioner's Toolkit, Wiley & Sons, 2009.
[25] R.D. Shanon, Revised Effective Ionic Radii and Systematic Studies of Interatomic Distances in Halides and Chalcogenides, Acta. Cryst. A 32 (1976) 751–767.
[26] N. Treuil, C. Labrugère, M. Menetrier, J. Portier, G. Campet, A. Deshayes, J.C. Frison, S.-J. Hwang, S.W. Song, J.-H. Choy, Relationship between Chemical Bonding Nature and Electrochemical Property of $LiMn_2O_4$ Spinel Oxides with Various Particle Sizes: "Electrochemical Grafting" Concept, Phys. Chem. B 103 (1999) 2100–2106.
[27] M.H. Alfaruqi, J. Gim, S. Kim, J. Song, J. Jo, S. Kim, V. Mathew, J. Kim, Enhanced Reversible Divalent Zinc Storage in a Structurally Stable α-MnO_2 Nanorod Electrode, J. Power. Sources 288 (2015) 320–327.
[28] S.-J. Hwang, D.H. Park, J.-H. Choy, G. Campet, Effect of Chromium Substitution on the Lattice Vibration of Spinel Lithium Manganate: A New Interpretation of the Raman Spectrum of $LiMn_2O_4$, J. Phys. Chem. B 108 (2004) 12713–12717.
[29] M. Sun, B. Lan, T. Lin, G. Cheng, F. Ye, L. Yu, X. Cheng, X. Zheng, Controlled Synthesis of Nanostructured Manganese Oxide: Crystalline Evolution and Catalytic Activities, CrystEngComm 15 (2013) 7010–7018.
[30] D.H. Park, S.-H. Lee, T.W. Kim, S.T. Lim, S.-J. Hwang, Y.S. Yoon, Y.-H. Lee, J.-H. Choy, Non-Hydrothermal Synthesis of 1D Nanostructured Manganese-Based Oxides: Effect of Cation Substitution on the Electrochemical Performance of Nanowires, Adv. Funct. Mater. 17 (2007) 2949–2956.
[31] J.E. Huheey, E.A. Keiter, R.L. Keiter, Inorganic Chemistry, fourth ed., Harper & Row, New York, 1980.
[32] K. Song, J. Jung, Y.-U. Heo, Y.C. Lee, K. Cho, Y.-M. Kang, α-MnO_2 Nanowire Catalysts with Ultra-high Capacity and Extremely Low Overpotential in Lithium – Air Batteries through Tailored Surface Arrangement, Phys. Chem. Chem. Phys. 15 (2013) 20075–20079.
[33] S. Hirai, S. Yagi, A. Seno, M. Fujioka, T. Ohno, T. Matsuda, Enhancement of the Oxygen Evolution Reaction in Mn^{3+}-based Electrocatalysts: Correlation between Jahn–Teller Distortion and Catalytic Activity, RSC Adv. 6 (2016) 2019–2023.
[34] U. Maitra, B.S. Naidu, A. Govindaraj, C.N.R. Rao, Importance of Trivalency and the e_g^1 Configuration in the Photocatalytic Oxidation of Water by Mn and Co Oxides, Proc. Natl. Acad. Sci. USA 110 (2013) 11704–11707.
[35] J. Ribeiro, G. Tremiliosi-Filho, P. Olivi, A. R. d. Andrade, XAS Characterization of the $RuO_2 - Ta_2O_5$ System Local (crystal) Structure, Mater. Chem. Phys. 125 (2011) 449–460.
[36] J.B. Condon, Surface Area and Porosity Determinations by Physisorption: Measurements and Theory, First Ed., Elsevier, Amsterdam, Boston, 2006.
[37] T. Allen, Powder Sampling and Particle Size Determination, First Ed., Elsevier, Amsterdam, Boston, 2003.
[38] J. Zhang, Z. Xia, L. Dai, Carbon-based Electrocatalysts for Advanced Energy Conversion and Storage, Sci. Adv. 1 (2015) e1500564.
[39] N. Ramaswamy, S. Mukerjee, Fundamental Mechanistic Understanding of Electrocatalysis of Oxygen Reduction on Pt and Non-Pt Surfaces: Acid versus Alkaline Media, Adv. Phys. Chem. 2012 (2012) 491604.
[40] Y. Zhu, W. Zhou, J. Yu, Y. Chen, M. Liu, Z. Shao, Enhancing Electrocatalytic Activity of Perovskite Oxides by Tuning Cation Deficiency for Oxygen Reduction and Evolution Reactions, Chem. Mater. 28 (2016) 1691–1697.
[41] T. Reier, M. Oezaslan, P. Strasser, Electrocatalytic Oxygen Evolution Reaction (OER) on Ru, Ir, and Pt Catalysts: A Comparative Study of Nanoparticles and Bulk Materials, ACS Catal. 2 (2012) 1765–1772.
[42] H.B. Yang, J. Miao, S.-F. Hung, J. Chen, H.B. Tao, X. Wang, L. Zhang, R. Chen, J. Gao, H.M. Chen, L. Dai, B. Liu, Identification of Catalytic Sites for Oxygen Reduction and Oxygen Evolution in N-doped Graphene Materials: Development of Highly Efficient Metal-free Bifunctional Electrocatalyst, Sci. Adv. 2 (2016) e1501122.
[43] S. Chen, J. Duan, M. Jaroniec, S.-Z. Qiao, Nitrogen and Oxygen Dual-doped Carbon Hydrogel Film as a Substrate-free Electrode for Highly Efficient Oxygen Evolution Reaction, Adv. Mater. 26 (2014) 2925–2930.
[44] Q. Zhang, Z.D. Wei, C. Liu, X. Liu, X.Q. Qi, S.G. Chen, W. Ding, Y. Ma, F. Shi, Y.M. Zhou, Copper-doped Cobalt Oxide Electrodes for Oxygen Evolution Reaction Prepared by Magnetron Sputtering, Int. J. Hydrogen Energy 37 (2012) 822–830.
[45] D. Jeong, K. Jin, S.E. Jerng, H. Seo, D. Kim, S.H. Nahm, S.H. Kim, K.T. Nam, Mn_5O_8 Nanoparticles as Efficient Water Oxidation Catalysts at Neutral pH, ACS Catal. 5 (2015) 4624–4628.
[46] C. Yang, O. Fontaine, J.-M. Tarascon, A. Grimaud, Chemical Recognition of Active Oxygen Species on the Surface of Oxygen Evolution Reaction Electrocatalysts, Angew. Chem. Int. Ed. 56 (2017) 8652–8656.
[47] E. Fabbri, M. Nachtegaal, T. Binninger, X. Cheng, B.-J. Kim, J. Durst, F. Bozza, T. Graule, R. Schäublin, L. Wiles, M. Pertoso, N. Danilovic, K.E. Ayers, T.J. Schmidt, Dynamic Surface Self-reconstruction is the Key of Highly Active Perovskite Nano-electrocatalysts for Water Splitting, Nat. Mater. 16 (2017) 925–932.
[48] H. Lv, S. Mu, N. Cheng, M. Pan, Nano-silicon Carbide Supported Catalysts for PEM Fuel Cells with High Electrochemical Stability and Improved Performance by Addition of Carbon, Appl. Catal., B. 100 (2010) 190–196.
[49] A. Wieckowski, and Applications, Interfacial Electrochemistry: Theory, Experiment, Marcel Dekker, Inc, New York, 1999.
[50] Y. Lee, J. Suntivich, K.J. May, E.E. Perry, Y. Shao-Horn, Synthesis and Activities of Rutile IrO_2 and RuO_2 Nanoparticles for Oxygen Evolution in Acid and Alkaline Solutions, J. Phys. Chem. Lett. 3 (2012) 339–404.
[51] S. Gadipelli, T. Zhao, S.A. Shevlin, Z. Guo, Switching Effective Oxygen Reduction and Evolution Performance by Controlled Graphitization of a Cobalt – Nitrogen – Carbon Framework System, Energy Environ. Sci. 9 (2016) 1661–1667.
[52] M. Prabu, K. Ketpang, S. Shanmugam, Hierarchical Nanostructured $NiCo_2O_4$ as an Efficient Bifunctional Non-precious Metal Catalyst for Rechargeable Zinc – Air Batteries, Nanoscale 6 (2014) 3173–3181.
[53] P. Tan, Z.H. Wei, W. Shyy, T.S. Zhao, X.B. Zhu, A Nano-structured RuO_2/NiO Cathode Enables the Operation of Non-aqueous Lithium – Air Batteries in Ambient Air, Energy Environ. Sci. 9 (2016) 1783–1793.
[54] InvestmentMine, http://www.infomine.com/investment/metal-prices/, 2016 (accessed 16.08).